Title	Third harmonic generation from mid-IR to near-IR regions in a phase-matched silicon-silicon-nanocrystal hybrid plasmonic waveguide
Author(s)	Wu, Tingting; Shum, Perry Ping; Shao, Xuguang; Huang, Tianye; Sun, Yunxu
Citation	Wu, T., Shum, P. P., Shao, X., Shao, X., Huang, T., & Sun, Y. (2014). Third harmonic generation from mid-IR to near-IR regions in a phase-matched silicon-silicon-nanocrystal hybrid plasmonic waveguide. Optics express, 22(20), 24367-23477.
Date	2014
URL	http://hdl.handle.net/10220/24538
Rights	© 2014 Optical Society of America. This is the author created version of a work that has been peer reviewed and accepted for publication by Optics Express, Optical Society of America. It incorporates referee's comments but changes resulting from the publishing process, such as copyediting, structural formatting, may not be reflected in this document. The published version is available at: [http://dx.doi.org/10.1364/OE.22.024367].

Third harmonic generation from mid-IR to near-IR regions in a phase-matched silicon-silicon-nanocrystal hybrid plasmonic waveguide

Tingting Wu,[1, 2,3] Perry Ping Shum,[1,2] Xuguang Shao,[1,2] Tianye Huang,[1,2] and Yunxu Sun[1, 2,3,*]

[1]*CINTRA CNRS/NTU/THALES, UMI 3288, 50 Nanyang Drive, Singapore*
[2]*School of Electrical and Electronics Engineering, Nanyang Technological University, Singapore*
[3]*Harbin Institute of Technology Shenzhen Graduate School, Shenzhen, China*
[*]*sunyunxu@hitsz.edu.cn*

Abstract: The conversion efficiency of third harmonic generation (THG) from mid-IR (3600 nm) to near-IR (1200 nm) regions in a silicon-silicon-nanocrystal hybrid plasmonic waveguide (SSHPW) was calculated. The required modal phase-matching condition (PMC) between the 0-th mode at fundamental wave (FW) and the 2-nd mode at third harmonic (TH) is achieved by carefully designing the waveguide geometry. Benefiting from the hybridized surface plasmon polariton (SPP) nature of the two guided modes, the SSHPW is capable of achieving both high THG nonlinear coefficient $|I_6|$ and reasonable linear propagation loss, thereby resulting in large figure-of-merits (FOMs) for both FW and TH. According to our simulation, THG conversion efficiency up to 0.823% is achieved at 62.9 μm SSHPW with pump power of 1 W.

OCIS codes: (070.4340) Nonlinear optical signal processing; (190. 2620) Harmonic generation and mixing; (250.5403) Plasmonics; (250.4390) Nonlinear optics, integrated optics.

References and links

1. W. R. Bosenberg, A. Drobshoff, J. I. Alexander, L. E. Myers, and R. L. Byer, "93% pump depletion, 3.5-W continuous-wave, singly resonant optical parametric oscillator," Opt. Lett. **21**(17), 1336-1338 (1996).
2. A. J. Henderson, P. M. Roper, L. A. Borschowa, and R. D. Mead, "Stable, continuously tunable operation of a diode-pumped doubly resonant optical parametric oscillator," Opt. Lett. **25**(17), 1264-1266 (2000).
3. M. E. Klein, D .H. Lee, J .P. Meyn, K. J. Boller, and R. Wallenstein, "Singly resonant continuous-wave optical parametric oscillator pumped by a diode laser," Opt. Lett. **24**(16), 1142-1144 (1999).
4. S. Y. Zhang, D. G. Revin, J. W. Cockburn, K. Kennedy, A. B. Krysa, and M. Hopkinson, "λ~3.1 μm room temperature InGaAs/AlAsSb/InP quantum cascade lases," Appl. Phys. Lett. **94**(3), 031106 (2009).
5. D. G. Revin, J. W. Cockburn, M. J. Steer, R. J. Airey, M. Hopkinson, A. B. Krysa, L. R. Wilson, and S. Menzel, "InGaAs/AlAsSb/InP quantum cascade lasers operating at wavelengths close to 3 μm," Appl. Phys. Lett. **90**(2), 021108 (2007).
6. A. Soibel, M. Wright, W. Farr, S. Keo, C. Hill, R. Q. Yang, and H. C. Liu, "Free space optical communication utilizing mid-infrared interband cascade laser," Proc. of SPIE **7587**, 75870S (2010).
7. N. S. Prasad, D. D. Smith, and J. R. Magee, "Data communication in mid-IR using a solid-state laser pumped optical parametric oscillator," Proc. of SPIE **4821**, 214-224 (2002).
8. B. Corcoran, C. Monat, M. Pelusi, C. Grillet, T. P. White, L. O'Faolain, T. F. Krauss, B. J. Eggleton, and D. J. Moss, "Optical signal processing on a silicon chip at 640Gb/s using slow-light," Opt. Express **18**(8), 7770-7781 (2010).
9. L. Canioni, M. Bellec, A. Royon, B. Bousquet, and T. Cardinal, "Three-dimensional optical data storage using third-harmonic generation in silver zinc phosphate glass," Opt. Lett. **33**(4), 360-362 (2008).
10. S. W. Chu, S. Y. Chen, G. W. Chern, T. H. Tsai, Y. C. Chen, B. L. Lin, and C. K. Sun, "Studies of $\chi^{(2)}$/ $\chi^{(3)}$ tensors in submicron-scaled bio-tissues by polarization harmonics optical microscopy," Biophys. J. **86**, 3914–3922 (2004).

11. T. Huang, X. Shao, Z. Wu, T. Lee, Y. Sun, H. Q. Lam, J. Zhang, G. Brambilla, and P. P. Shum, "Efficient one-third harmonic generation in highly Germania-doped fibers enhanced by pump attenuation," Opt. Express **21**(23), 28403-28413 (2013).
12. V. Grubsky and A. Savchenko, "Glass micro-fibers for efficient third harmonic generation," Opt. Express **13**(18), 6798-6806 (2005).
13. T. Lee, Y. Jung, C. A. Codemard, M. Ding, N. G. R. Broderick, and G. Brambilla, "Broadband third harmonic generation in tapered silica fibres," Opt. Express **20**(8), 8503-8511 (2012).
14. A. Lin, A. Ryasnyanskiy, and J. Toulouse, "Tunable third-harmonic generation in a solid-core tellurite glass fiber," Opt. Lett. **36**(17), 3437-3439 (2011).
15. T. Chen, W. Gao, M. Liao, Z. Duan, D. Deng, M. Matsumoto, T. Misumi, T. Suzuki, and Y. Ohishi, "Tunable third-harmonic generation in a chalcogenide-tellurite hybrid optical fiber with high refractive index difference," Opt. Lett. **39** (4), 1005-1007 (2014).
16. J. Levy, M. A. Foster, A. L. Gaeta, and M. Lipson, "Harmonic generation in silicon nitride ring resonators," Opt. Express **19**(12), 11415-11421 (2011).
17. C. Monat, C. Grillet, B. Corcoran, D. J. Moss, B. J. Eggleton, T. P. White, and T. F. Krauss, "Investigation of phase matching for third-harmonic generation in silicon slow light photonic crystal waveguides using Fourier Optics," Opt. Express **18**(7), 6831-6840 (2010).
18. S. V. Afshar, M. A. Lohe, T. Lee, T. M. Monro, and N. G. R. Broderick, "Efficient third and one third harmonic generation in nonlinear waveguides," Opt. Lett. **38**(3), 329-331 (2013).
19. R. F. Oulton, V. J. Sorger, T. Zentgraf, R. M. Ma, C. Gladden, L. Dai, G. Bartal and X. Zhang, "Plasmon lasers at deep subwavelength scale," Nature **461**(7264), 629–632 (2009).
20. V. J. Sorger, Z. Ye, R. F. Oulton, Y. Wang, G. Bartal, X. Yin and X. Zhang, "Experimental demonstration of low-loss optical waveguiding at deep sub-wavelength scales," Nature Commun. **2**(331), (2011).
21. A. V. Krasavin and A. V. Zayats, "Silicon-based plasmonic waveguides," Opt. Express **18**(11), 11791–11799 (2010).
22. L. Chen, J. Shakya, and M. Lipson, "Subwavelength confinement in an integrated metal slot waveguide on silicon," Opt. Lett. **31**(14), 2133–2135 (2006).
23. F. F. Lu, T. Li, J. Xu, Z. Xie, L. Li, S. Zhu, and Y. Zhu, "Surface plasmon polariton enhanced by optical parametric amplification in nonlinear hybrid waveguide," Opt. Express **19**(4), 2858-2865 (2011).
24. F. M. Pigozzo, D. Modotto, and S. Wabnitz, "Second harmonic generation by modal phase matching involving optical and plasmonic modes," Opt. Lett. **37**(12), 2244-2246 (2012).
25. J. Zhang, E. Cassan, and X. Zhang, "Efficient second harmonic generation from mid-infrared to near-infrared regions in silicon-organic hybrid plasmonic waveguides with small fabrication-error sensitivity and a large bandwidth," Opt. Lett. **38**(12), 2089-2091 (2013).
26. P. Sanchis, J. Blasco, A. Martinez and J. Martì, "Design of Silicon-Based Slot Waveguide Configurations for Optimum Nonlinear Performance," J. Lightwave Technol. **25**(5), 1298-1305 (2007).
27. A. Martinez, J. Blasco, P. Sanchis, J. V. Galan, J. Garcia-Ruperez, E. Jordana,n P. Gautier, Y. Lebour, S. Hernandez, R. Spano, R. Guider, N. Daldosso, B. Garrido, J. M. Fedeli, L. Pavesi and J. Marti, "Ultrafast all-optical switching in a silicon-nanocrystal-based silicon slot waveguide at telecom waveguides," Nano Lett., **10**(4), 1506-1511 (2010).
28. P. B. Johnson, and R. W. Christy, "Optical constants of the noble metals," Phys. Rev. B **6**(12), 4370-4379 (1972).
29. R. Spano, J. V. Galan, P. Sanchis, A. Martinez, J. Mart ί and L. Pavesi, "Group velocity dispersion in horizontal slot waveguides filled by Si nanocrystals," International Conf. on Group IV Photonics, 314-316 (2008).
30. L. Zhang, Y. Yue, R. G. Beausoleil, and A. E. Willner, "Flattened dispersion in silicon slot waveguides," Opt. Express **18**(19), 20529-20534 (2010).
31. D. Edwards and E. Ochos, "Infrared refractive index of silicon," Appl. Opt. **19**(24), 4130-4131 (1980).
32. H. malitson, "Interspecimen comparison of the refractive index of fused silica," J. Opt. Soc. Am. **54**(11), 1401 (1964).
33. T. Wu, Y. Sun, X. Shao, P. P. Shum, and T. Huang, "Efficient phase-matched third harmonic generation in an asymmetric plasmonic slot waveguide," Opt. Express **22**(15), 18612-18624 (2014).
34. G. J. Hawkins, "Spectral characteristics of infrared optical materials and filters," Ph.D. thesis (University of Reading, 1998).
35. S. Sakaguchi, and S. Todoroki, "Optical properties of GeO_2 glass and optical fibers," Appl. Opt. **36**(27), 6809-6811 (1997).
36. C. Ciminelli, V. M. N. Passaro, F. Dell'Olio, and M. N. Armenise, "Three-dimensional modelling of scattering loss in InGaAsP/InP and silica-on-silicon bent waveguides," J. Eur. Opt. Soc. Rapid Publ. **4**, 1-6 (2009).
37. F. Grillot, L. Vivien, E. Cassan, and S. Laval, "Influence of waveguide geometry on scattering loss effects in submicron strip silicon-on-insulator waveguides," IET Optoelectron. **2**(1), 1-5 (2008).
38. Q. Lin, J. Zhang, G. Piredda, R. W. Boyd, P. M. Fauchet, and G. P. Agrawal, "Dispersion of silicon nonlinearities in the near infrared region," Appl. Phys. Lett. **91**(2), 02111 (2007).
39. R. B. Boyd, *Nonlinear Optics, Second Edition*, (Academic 2003).
40. L. Pavesi, and R. Turan, *Silicon Nanocrystals: Fundamentals, Synthesis and Applications* (Academic, 2010), Chap. 2.

41. T. Wang, N. Venkatram, J. Gosciniak, Y. Cui, G. Qian, W. Ji, and D. T. H. Tan, "Multi-photo absorption and third-order nonlinearity in silicon at mid-infrared wavelengths" Opt. Express **21**(26), 32192-32198 (2013).
42. J. Matres, C. Lacava, G. C. Ballesteros, P. Minzioni, I. Cristiani, J. M. F ́ed ́eli, J. Mart î and C. J. Oton, "Low TPA and free-carrier effects in silicon nanocrystal-based horizontal slot waveguides,"" Opt. Express **20**(21), 23838-23845 (2012).
43. J. Renger, R. Quidant, and L. Novotny, "Enhanced nonlinear response from metal surfaces," Opt. Express **19**(3), 1777-1785 (2011).
44. P. Ginzburg, A. Hayat, N. Berkovitch, and M. Orenstein, "Non-local ponderomotive nonlinearity in plasmonics," Opt. Lett. **35**(10), 1551-1553 (2010).

1. Introduction

Recently, the emerging field of mid-IR photonics is motivating more and more research interest owing to their potential applications in a wide variety of areas, including free-space communications, chemical or biological sensors, environmental monitors, IR countermeasures and medical procedures. Besides, current mature development of compact, low-cost mid-IR light sources [1-5], together with their wide range applications in optical communications [6, 7], has pursued further investigation of mid-IR based techniques. On the other hand, third harmonic generation (THG) devices working in this special waveband, can find promising applications in the area of signal processing due to the well-accepted free-space optical communications in the atmospheric transmission windows (3-5 and 8-14 μm). THG has also been demonstrated as a versatile tool in realizing the high speed optical performance monitoring of in-band optical signal-to-noise ratio (OSNR) and residual dispersion [8], three-dimensionally storing optical data [9] and studying the biological materials [10]. Therefore, the mid-IR sources based third-order frequency conversion opens a new realm of nonlinear interactions. Nevertheless, little THG experiment or analytical modeling on THG has been reported.

Typically, high THG efficiency in a waveguide platform depends on three key aspects, including large third-order nonlinear coefficient of the nonlinear interactive material, modal phase-matching condition (PMC) and sufficient pump-harmonic modal overlap. To achieve high THG efficiency, different artificial structures have been explored and studied. For example, the advantage of THG in the Germania-doped fibers is the long interactive length, but the pump-harmonic modal overlap between the phase-matched modes is too small [11]. Silica microfiber is considered to be a promising candidate to obtain PMC between HE_{11} at fundamental wave (FW) and HE_{12} at third harmonic (TH) with greatly improved pump-harmonic modal overlap compared with the highly Germania-doped fibers. But the short interactive length and small third-order nonlinear coefficient result in limited conversion efficiency [12, 13]. Recently, various nonlinear materials with large nonlinear coefficients are also employed as platforms for THG [14, 15]. However, further work is still required to achieve PMC along with a large pump-harmonic modal overlap. By utilizing the slow light effect in silicon photonic crystal waveguide [8] and resonant effect in silicon nitride ring resonator [16], the interaction between the FW and the TH can be significantly enhanced. However, in the slow light waveguide, the FW mode can only phase-matched to the radiation mode or the leaky mode at TH [17], and PMC in the silicon nitride resonator is achieved between the 0-th mode at FW and the 18-th mode at TH. Accordingly, they all suffer from the drawback of small pump-harmonic modal overlap.

Although it has been theoretically predicted to be possible to achieve the three key aspects simultaneously [18], designing waveguides still remains to be a major challenge. Among the various proposed planar plasmonic structures, hybrid plasmonic waveguides, consisting of nanometer scale low-index layers integrated between metal layers and high-index silicon slabs, have been demonstrated to be able to provide tight field confinement and good mode enhancement with low linear propagation loss [19, 20]. The combination of the properties of metallic structures and silicon components promises a great mode confinement [21, 22], which provides opportunities for the nonlinear applications. For example, hybrid plasmonic

waveguide structures have utilized to study the second harmonic generation [23-25]. Additionally, PMC along with large pump-harmonic modal overlap can be obtained simultaneously by properly employing the waveguide geometry and the nonlinear interactive material. Based on these features, hybrid plasmonic waveguide structures are of huge potential to realize THG waveguide devices. For the choice of the main interactive material, silicon-nanocrystal (Si-nc), which possesses a high third-order nonlinear coefficient (one order of magnitude higher than silicon), is a promising candidate. It has been investigated in all-optical signal processing and optical switching [26, 27]. Second, this material can be produced using standard methods such as plasma enhanced chemical vapor deposition.

In this paper, we mainly study the performance of the phase-matched THG from mid-IR (3600 nm) to near-IR (1200 nm) regions in a silicon-silicon-nanocrystal (Si-Si-nc) hybrid plasmonic waveguide (SSHPW). The PMC between the 0-th mode at FW and the 2-nd mode at TH can be satisfied by properly engineering the waveguide geometry. Due to the hybridized surface plasmon polariton (SPP) nature of the two guided modes, high THG nonlinear coefficient $|I_6|$ and reasonable linear propagation loss are achieved, thereby leading to large figure-of-merits (FOMs) for both FW and TH. The THG performance in the SSHPW is analyzed by numerical simulations.

2. Waveguide structure and nonlinear modeling approach

The proposed structure in this paper is a silicon-silicon-nanocrystal (Si-Si-nc) hybrid plasmonic waveguide (SSHPW) at the operating wavelength of 3600 nm, as presented in Fig. 1. The width and height of the Si-nc slot are w and h. The heights of the metal layer, silicon slab and silica substrate are h_m, h_{si} and h_{SiO2}. Metal is selected to be silver (Ag) due to its relatively low induced linear propagation loss and its permittivity dispersion is given in [28]. Besides of silver, three other metals, gold, copper and platinum, can also be used. The considered Si-nc with linear refractive indices of n (3600 nm) = 1.7166, n (1200 nm) = 1.7248 [29] and third-order nonlinear coefficient of $n_2 = 4.8\times10^{-17}$ m^2/W at 1550 nm [30] is integrated into the slot region as the main interactive nonlinear material. Material dispersions of silicon (Si) [31] and silica (SiO_2) [32] are taken into account. The whole device is surrounded by air. A possible flow to fabricate the waveguide is as following. First, deposition of SiO_2, Si and Si-nc can be done on a Si wafer using plasma enhanced chemical vapor deposition. Then deposit another SiO_2 as a hard mask layer on the Si-nc layer, followed by sputtering electron beam (Ebeam) resist layer as a mask and then patterned utilizing Ebeam lithography. The pattern of the Ebeam resist layer can be transferred to hard mask layer (SiO_2) by reactive ion etching. Remove the Ebeam resist layer, and the pattern of the hard mask layer can transfer to Si-nc and Si layers before removing. Finally the silver layer can be deposited on top by sputtering.

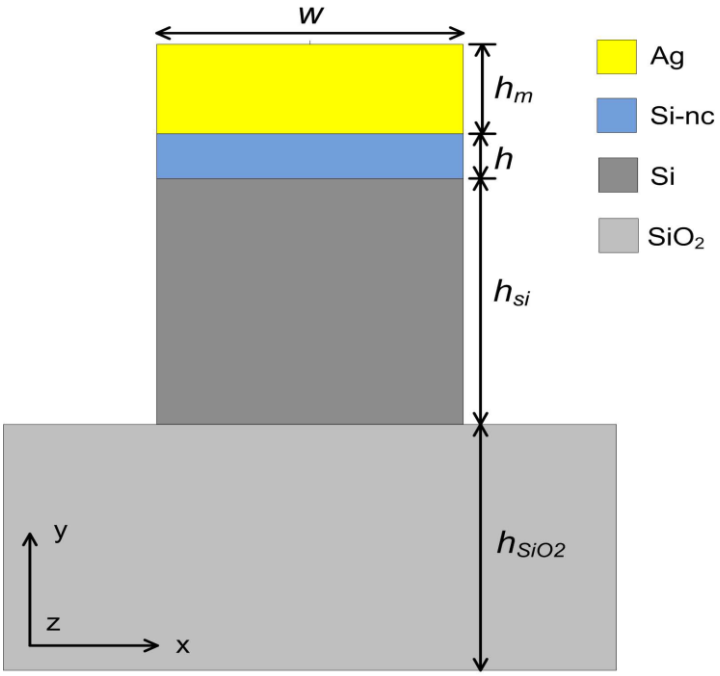

Fig. 1. Cross-section view of the proposed nonlinear silico-silicon-nanocrystal (Si-Si-nc) hybrid plasmonic waveguide (SSHPW).

Attenuation of optical waves strongly impairs the devices performance. During our calculation, the linear attenuation of the waveguide device is contributed by the extrinsic and intrinsic losses. Extrinsic loss is due to the device sidewall roughness, namely surface scattering loss, while the intrinsic loss is induced by material absorption. In order to correctly model the mid-IR THG performance in the proposed lossy SSPHW, the nonlinear coupled differential equations describing the interaction between the two guided modes can be derived as [33]:

$$\frac{\partial A_1}{\partial z} = -\frac{\alpha_1}{2}A_1 - \frac{\alpha_a(\vec{r}_\perp)}{2}A_1 + i[(I_1|A_1|^2 + I_2|A_3|^2)A_1 + I_3(A_1^*)^2 A_3 e^{i\delta\beta z}] \quad (1)$$

$$\frac{\partial A_3}{\partial z} = -\frac{\alpha_3}{2}A_3 - \frac{\alpha_s(\vec{r}_\perp)}{2}A_3 + i[(I_4|A_1|^2 + I_5|A_3|^2)A_3 + I_6(A_1)^3 e^{-i\delta\beta z}] \quad (2)$$

where j = 1 refers to the FW, j = 3 refers to the TH, A_j represent the slowly varying portion of the complex electric fields, β_j are the phase propagation constant. $\alpha_j = \frac{40\pi\,\mathrm{Im}(n_{effj})}{\lambda_j}\log e$, $\alpha_a(\vec{r}_\perp)$ and $\alpha_s(\vec{r}_\perp)$ are the linear propagation loss coefficients induced by the metal layer, silica absorption, and sidewall roughness, respectively. $\delta\beta=\beta_3-3\beta_1$ is the phase mismatch. Note that, the linear absorption loss in the silicon slab region is neglected due to the loss-free transmission window from 1.2 to 6 μm [34]. For the silica substrate, the absorption loss coefficient α_a is 4×10^{-4} dB/μm at FW and 0 at TH, respectively [35]. The surface scattering loss coefficient α_s is assumed to be 2×10^{-4} dB/μm for TH [36, 37]. The nonlinear coefficients I_i (i = 1, 2⋯, 6) are related to the modal overlap integrals between the fundamental and third harmonic waves which are defined as follows:

$$I_1 = \frac{1}{12}\mathrm{k}_1 \cdot n_0^2(\omega_1, \vec{r}_\perp)\cdot \mathrm{n}_2(\omega_1, \vec{r}_\perp)\iint_{A_{NL}}(2|\vec{F}_1|^4 + |\vec{F}_1^2|^2)dS \quad (3)$$

$$I_2 = \frac{1}{6}\mathrm{k}_1 \cdot n_0^2(\omega_1, \vec{\mathrm{r}}_\perp) \cdot \mathrm{n}_2(\omega_1, \vec{\mathrm{r}}_\perp) \iint_{A_{NL}} (\left|\vec{\mathrm{F}}_1\right|^2 \left|\vec{\mathrm{F}}_3\right|^2 + \left|\vec{\mathrm{F}}_1 \cdot \vec{\mathrm{F}}_3\right|^2 + \left|\vec{\mathrm{F}}_1 \cdot \vec{\mathrm{F}}_3^*\right|^2) dS \quad (4)$$

$$I_3 = \frac{1}{4}\mathrm{k}_1 \cdot n_0^2(\omega_1, \vec{\mathrm{r}}_\perp) \cdot \mathrm{n}_2(\omega_1, \vec{\mathrm{r}}_\perp) \iint_{A_{NL}} (\vec{\mathrm{F}}_1^* \cdot \vec{\mathrm{F}}_3)(\vec{\mathrm{F}}_1^* \cdot \vec{\mathrm{F}}_1^*) dS \quad (5)$$

$$I_4 = \frac{1}{2}\mathrm{k}_1 \cdot n_0^2(\omega_3, \vec{\mathrm{r}}_\perp) \cdot \mathrm{n}_2(\omega_3, \vec{\mathrm{r}}_\perp) \iint_{A_{NL}} (\left|\vec{\mathrm{F}}_1\right|^2 \left|\vec{\mathrm{F}}_3\right|^2 + \left|\vec{\mathrm{F}}_1 \cdot \vec{\mathrm{F}}_3\right|^2 + \left|\vec{\mathrm{F}}_1 \cdot \vec{\mathrm{F}}_3^*\right|^2) dS \quad (6)$$

$$I_5 = \frac{1}{4}\mathrm{k}_1 \cdot n_0^2(\omega_3, \vec{\mathrm{r}}_\perp) \cdot \mathrm{n}_2(\omega_3, \vec{\mathrm{r}}_\perp) \iint_{A_{NL}} (2\left|\vec{\mathrm{F}}_3\right|^4 + \left|\vec{\mathrm{F}}_3^2\right|^2) dS \quad (7)$$

$$I_6 = \frac{1}{4}\mathrm{k}_1 \cdot n_0^2(\omega_3, \vec{\mathrm{r}}_\perp) \cdot \mathrm{n}_2(\omega_3, \vec{\mathrm{r}}_\perp) \iint_{A_{NL}} (\vec{\mathrm{F}}_1^* \cdot \vec{\mathrm{F}}_3)(\vec{\mathrm{F}}_1^* \cdot \vec{\mathrm{F}}_1^*) dS \quad (8)$$

in which $n_2(\omega_j, \vec{\mathrm{r}}_\perp)$ is the third-order nonlinear coefficients at any location of the waveguide, $k_1 = 2\pi/\lambda_1$ is the wave number, $n_0(\omega_j, \vec{\mathrm{r}}_\perp)$ is the linear refractive indices, $\vec{\mathrm{F}}_j$ are the power-normalized electric field distributions, and A_{NL} is the cross-section area of the waveguide. The THG nonlinear coefficient, I_6, is determined by the pump-harmonic modal overlap as shown in Eq. (8), which is used to evaluate the contribution of the two interactive modes, and directly influences the strength of the power transfer from FW to TH.

Note that the THG nonlinear process is based on the third-order nonlinear susceptibility $\chi^{(3)}$ which also leads to TPA. The real and imaginary parts of $\chi^{(3)}$ are relevant to the third-order nonlinear coefficient n_2 and the TPA coefficient α_2 by $\frac{\omega}{c} n_2 + \frac{i}{2}\alpha_2 = \frac{3\omega}{4\varepsilon_0 c^2 n_0^2}\chi^{(3)}$ [38]. The frequencies of the optical waves during the nonlinear optical interactions are much smaller than the lowest resonance frequency of the Si-nc. The third order nonlinear susceptibility ($\chi^{(3)}$) under these conditions is essentially independent of frequency [39]. Typically, it is valid to assume the third-order nonlinear coefficient of Si-nc to be constant over the wavelength range from 1200 nm to 3600 nm [39, 40]. The nonlinear refractive indices for Si-nc and silicon are n_2 (Si-nc) = 4.8×10^{-17} m^2/W [32], n_2 (Si, 3600 nm) = 4.5×10^{-18} m^2/W and n_2 (Si, 1200 nm) = 7×10^{-18} m^2/W [41], respectively. The TPA coefficients are assumed to be 0 at FW for Si-nc, silicon and silica. While the nonlinear loss due to the nonzero TPA coefficient at TH in the third order interaction process may limit the maximum achievable power lever of the TH. For the generated TH, the change of its power $P_3(z)$ along the z propagation direction is given by the following differential equation [42]:

$$\frac{dP_3(\mathrm{z})}{dz} = -\alpha_3 P_3(\mathrm{z}) + 2\,\mathrm{Im}\{\gamma\} P_3^2(\mathrm{z}) + 2I_6 P_1^{\frac{3}{2}}(\mathrm{z}) P_3^{\frac{1}{2}}(\mathrm{z}) \sin\Psi \quad (9)$$

where $\mathrm{Im}\{\gamma\}$ is the imaginary part of the nonlinearity parameter and represents the nonlinear loss, $P_j(\mathrm{z}) = \left|A_j(\mathrm{z})\right|^2$, and $\Psi = \delta\beta z + \varphi_3 - 3\varphi_1$. Therefore, nonlinear loss induced by TPA is strongly dependent on the power level of the generated TH. We restrict our analysis within relatively small pumping level (1 W) so that TPA can have very little impact on the value of the TH power. According to our calculation in fact, the weak power of the TH experiences negligible TPA induced nonlinear loss. It is known that 3PA happens when the energy of photos exceeds one third of the band gap $E_g/3$, where $E_g/3$ corresponds to a wavelength of 3.3 μm for silicon. Then the 3PA effect in silicon on the input pump wave can be neglected. 4PA happens in silicon when the energy of photos exceeds one fourth of the band gap $E_g/4$ which corresponds to a wavelength of 4.4 μm. Therefore, 4PA becomes the

dominant nonlinear optical effect at 3600 nm. T. Wang et al. derived the 4PA coefficient of silicon using the open aperture Z-scan method [41]. However, the 4PA coefficient of silicon is too much small at 3600 nm ($\sim 5\times10^{-51}$ m^5/W^3) compared with the linear propagation loss coefficients. On the other hand, we have restricted our analysis within relatively small pumping level (1 W). Accordingly, the nonlinear loss induced by 4PA in silicon slab region is also negligible.

To realize high THG efficiency, one of the most important issues is the PMC which requires $\delta\beta \approx 0$. The other key issue is achieving large THG nonlinear coefficient I_6. In the following section, the waveguide design for these two purposes is discussed in details.

3. PMC and THG performance

During the calculation, with fixed slot width *w*, slot height *h*, silver layer height h_m, and silica substrate height at 240 nm, 40 nm, 100 nm, and 500 nm, the silicon slab height h_{si} is adjusted to fulfill the PMC. Note that, the slot width is fixed to be 240 nm in the present work for convenience. According to our simulation, PMC can be achieved between the 0-th waveguide mode at FW and the 2-nd waveguide mode at TH. We did not find any other modes at TH which could phase-match with the FW. We obtain the effective index as a function of the silicon slab height using the full-vector finite-element mode analysis method based commercial software COMSOL. The results are plotted in Fig. 2(a). Both of the two mode indices increase with increasing the silicon slab height. The intersection point at the silicon slab height of 510 nm represents the phase-matching point where the refractive indices of the two modes are 1.627816+0.005174i and 1.627853+0.001665i, respectively. Therefore, it is possible to tune the phase-matching condition experimentally through varying the silicon slab height under other fixed waveguide geometric parameters. It needs to be stressed that, the propagation loss coefficient $\alpha_j = \frac{40\pi \,\mathrm{Im}(n_{effj})}{\lambda_j}\log e$ induced by the silver layer is over two orders of magnitude larger than α_a and α_s. Figures 2(b) and 2(c) give the corresponding 2D dominant field component *Ey* distributions. Obviously, for the 0-th mode at FW, the electrical components in the waveguide are all positive, while the 2-nd mode at TH preserves both positive and negative parts which contribution oppositely to the THG nonlinear coefficient as discussed above. However, in the SSHPW the positive part of the 2-nd mode is mainly localized in the slot region while the negative part is mainly localized in the silicon slab region leading to large pump-harmonic modal overlap. That is the attraction of the hybrid waveguide structure for performing third-order frequency conversion.

To more clearly illustrate the property of the modal overlap between the 0-th mode at FW and the 2-nd mode at TH, we also plot the 1 D field distributions in Fig. 3 along the *y* cutline [dash lines shown in Figs. 2(b) and 2(c)], which illustrates that the electric field at FW almost does not penetrate inside the silver layer. Although metal benefits from strong third-order optical nonlinearity at optical frequencies, its practical exploitation is limited by the weak penetration of the electric fields within the metal and the screening by the surface charges [43]. The driving field which supposed to enter the metal is prevented due to the screening of the electromagnetic field by the surface charges at the metal-dielectric interface and the exponential decay [43, 44]. The generation of the nonlinear response is inhibited accordingly because of the limited volume contribution by the metal's skin depth. Therefore, the nonlinear process of THG in the silver layer or at the silver surface can be rationally neglected. We can see that there are two changes of sign in the silicon part for the 2-nd mode at TH. More electromagnetic energy will concentrate in the silicon region with larger silicon slab area resulting in lower linear propagation loss induced by silver since the field penetrated inside the metal layer is further decreased. The guided hybridized mode is the result of the strong coupling between the SPP mode in the Si-nc slot region and the dielectric mode in the silicon

slab region. Specifically, the 0-th mode at FW results from the coupling between the SPP and the TM_{00} dielectric modes. While the 2-nd mode at TH results from the coupling between the SPP and the TM_{02} dielectric modes with more field concentrated inside the silicon part. Therefore, the 2-nd mode has lower linear propagation loss. It needs to be stressed here that the hybridized SPP mode has much smaller loss than the pure SPP one.

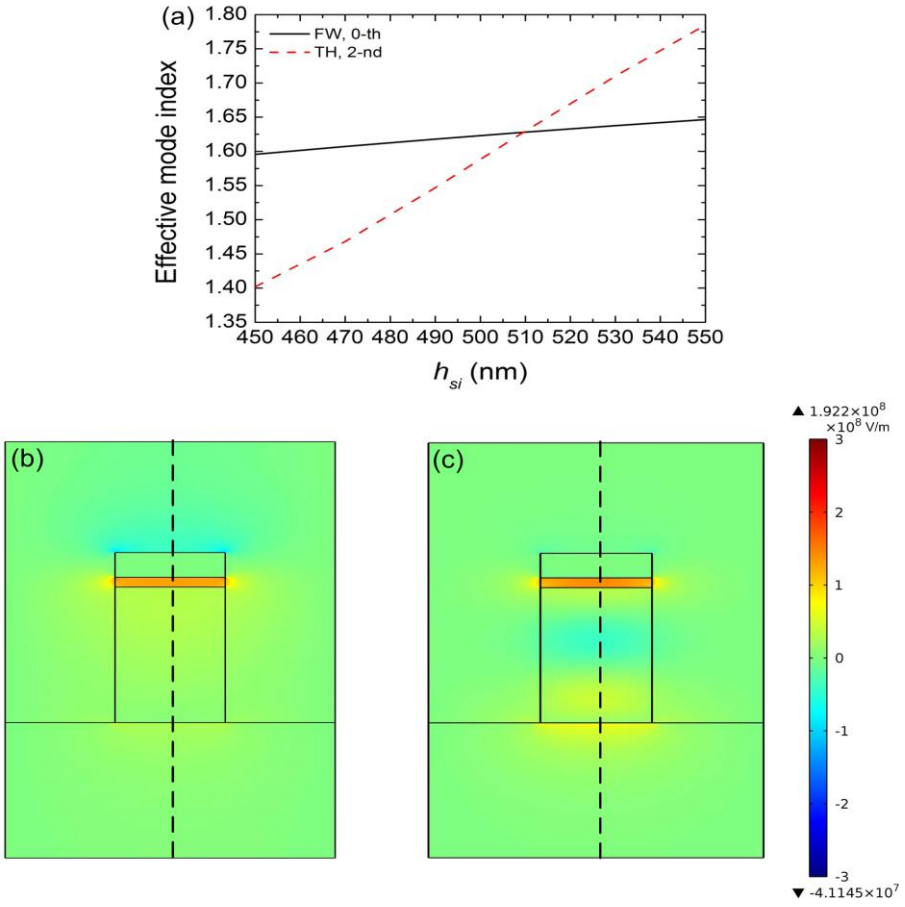

Fig. 2. (a) Effective mode indices of the 0-th mode at FW and the 2-nd mode at TH as a function of the silicon slab height h_{Si}; the corresponding 2D dominant field component *Ey* distributions of the (b) 0-th mode at FW, and (c) 2-nd mode at TH.

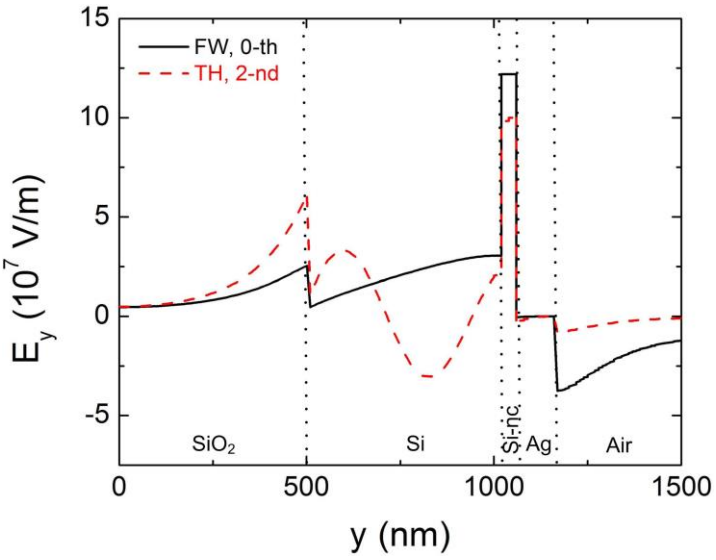

Fig. 3. 1D Ey distributions along y cutline [as the dash lines shown in Figs. 2(a) and 2(b)].

Then we optimize the waveguide geometry since the mere achieved PMC is not sufficient for achieving high THG efficiency. Another key factor is pump-harmonic modal overlap which links to the THG nonlinear coefficient I_6. The waveguide geometry is characterized by five geometrical parameters, the slot width w, slot height h, silver layer height h_m, silicon slab height h_{Si} and silica substrate height h_{SiO2}. These parameters should be properly designed so as to maximize the resulting I_6 along with reasonable linear propagation loss. The silicon slab height as a function of the slot height at different PMCs is graphed in Fig. 4(a) with fixed slot width, silver layer height and silica substrate height at 240 nm, 100 nm and 500 nm. It can be found that, the silicon slab height decreases with the increase of the slot height to obtain PMC because more optical power at TH concentrates into the silicon slab region with larger slot while optical power distribution at FW is much less influenced. I_6 is the THG nonlinear coefficient to evaluate the contribution of the two interactive modes, which is responsible for high THG efficiency. Note that, the non-zero pump-harmonic modal overlap can lead to I_6 building up. It is important to emphasis that I_6 is complex due to the complex mode fields. During our calculation, only increasing the absolute value of the imaginary part of I_6 can enlarge the THG conversion efficiency. Therefore, we evaluate the absolute value of I_6, i.e. $|I_6|$. The linear propagation loss is another crucial factor since less power of FW can be transferred to TH with higher loss. Therefore, to select one waveguide structure at PMC condition to generate the highest THG efficiency, we carried out an optimization of the waveguide geometric parameters to achieve the largest THG nonlinear coefficient $|I_6|$ with moderate linear propagation loss coefficient. We define the FOM to evaluate the performance at different PMC points as FOM_FW, TH = $|I_6|/\alpha_{FW,\,TH}$, where $\alpha_{FW} = \alpha_1+\alpha_a$ and $\alpha_{TH} = \alpha_3+\alpha_s$ are the linear propagation losses at FW and TH, respectively. The calculated $|I_6|$ and the corresponding linear propagation loss for various slot heights at different PMCs are plotted in Fig. 4(b). A larger silicon slab height is needed to satisfy the PMC, which enhances the dielectric-like feature of the hybridized modes. As a result, the propagation loss variation becomes flatter, as shown in Fig. 4(b). From Fig. 4(c) we can find that both FOM_FW and FOM_TH increase first and then decrease when the slot height h gets larger. The nonmonotonic behavior of the FOMs results from the combined effects of $|I_6|$ and linear

propagation loss. When the slot height is around 70 nm, the $|I_6|$ over the linear propagation loss are relatively larger, which corresponds to greater FOMs for both FW and TH. When the slot height is larger than 70 nm, the increased slot area becomes the dominant factor, consequently leading to dramatic reduction of $|I_6|$ along with moderate reduction of the linear propagation loss. Therefore, the most efficient waveguide slot height is 70 nm, with corresponding FOM_FW = 0.0626 $W^{-1}dB^{-1}$ and FOM_TH = 0.065 $W^{-1}dB^{-1}$.

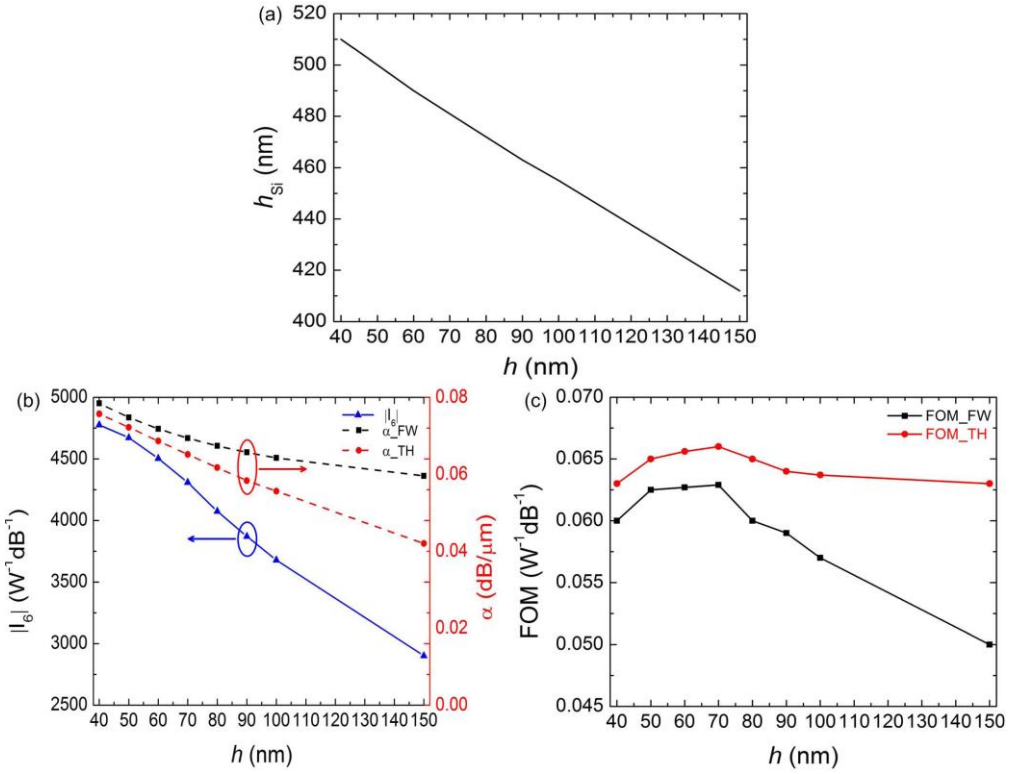

Fig. 4. (a) Silicon slab height h_{Si}, (b) pump-harmonic modal overlap related $|I_6|$ and the corresponding linear propagation loss, and (c) FOMs as a function of the slot height at different PMCs.

Finally, we numerically calculate Eqs. (1) and (2) using the Runge-Kutta method to investigate the THG conversion efficiency. During the simulation, the slot width, slot height, silver layer height, silicon slab height and silica substrate height are set at 240 nm, 70 nm, 100 nm, 481 nm and 500 nm, respectively. The input pump power is fixed to be 1 W. For the lossy interaction, the conversion efficiency to the third harmonic is defined as $\eta = P_3(Lp)/P_1(0)$, where $P_1(0) = |A_1(0)|^2$ is the input pump power, Lp is the waveguide length when the output power of the third harmonic reaches to its maximum value $P_3(Lp) = |A_3(Lp)|^2$. The power evaluation curves of P_1 and P_3 along the propagation distance are plotted in Fig. 5(a). For the 0-th mode at FW, its power monotonously decreases to the third-order conversion process and its linear propagation loss. The 2-nd mode at TH reaches to its maximum power up to 8.23 mW at a waveguide length of 62.9 μm. The corresponding conversion efficiency is 0.823% indicating that the SSHPW has the potential to realize THG devices with small footprint. Only these two modes experience the significant power exchange because all other harmonic modes are far from phase-matched. Next, to verify

that the geometry optimized waveguide structure can be used to achieve the highest THG efficiency, we further calculate the THG conversion efficiency with different waveguide structures. The inset of Fig. 5(b) shows the achievable conversion efficiency and the corresponding waveguide length with respect to the slot height at different PMCs with a fixed pump power of 1 W. It is no surprise that the efficiency curve matches well with the FOM curves depicted in Fig. 4(c). The waveguide length increases monotonically due to less propagation loss with lager slot area. Clearly, we can conclude that slot height at 70 nm under the PMC condition truly leads to higher conversion efficiency.

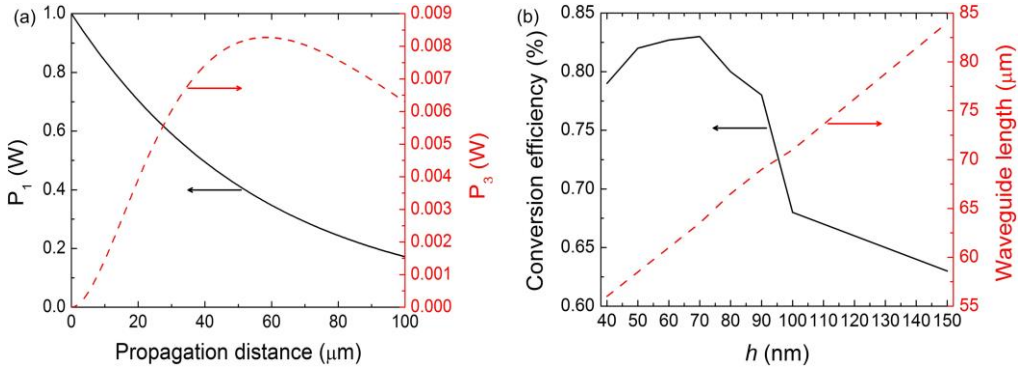

Fig. 5. Fixed the pump power to be 1 W, (a) optical powers of FW and TH along the propagation distance, (b) conversion efficiency and the corresponding waveguide length versus the slot height h under PMCs.

4. Conclusion

In conclusion, we propose a nonlinear silicon-silicon-nanocrystal hybrid plasmonic waveguide (SSHPW) with tight field confinement, good mode enhancement and reasonable linear propagation loss. Firstly, by optimizing the waveguide geometrical parameters, PMC between the 0-th mode at fundamental wave (FW) and the 2-nd mode at third harmonic (TH) can be achieved. Secondly, the influences of the geometry on several important factors during the THG process were analyzed in details. Finally, with input pump power of 1 W, THG conversion efficiency up to 0.823% is achieved at 62.9 μm SSHPW. Therefore, the capability of supporting THG within short waveguide length makes the SSHPW potential for future highly integrated nanophotonic circuits.

Acknowledgments：

This work was supported by the Singapore A*STAR SERC Grant: “Advanced Optics in Engineering” Program (Grant No. 1223600001).